

Automatic ultrasound vessel segmentation with deep spatiotemporal context learning

Baichuan Jiang^{1,2,†}, Alvin Chen^{1,†}, Shyam Bharat¹, and Mingxin Zheng¹

¹ Philips Research North America, 222 Jacobs St. Cambridge, MA 02141, USA
 {alvin.chen, shyam.bharat, mingxin.zheng}@philips.com

² *Department of Computer Science, Johns Hopkins University, Baltimore, MD 21218, USA bcjiang@jhu.edu

Abstract. Accurate, real-time segmentation of vessel structures in ultrasound image sequences can aid in the measurement of lumen diameters and assessment of vascular diseases. This, however, remains a challenging task, particularly for extremely small vessels that are difficult to visualize. We propose to leverage the rich spatiotemporal context available in ultrasound to improve segmentation of small-scale lower-extremity arterial vasculature. We describe efficient deep learning methods that incorporate temporal, spatial, and feature-aware contextual embeddings at multiple resolution scales while jointly utilizing information from B-mode and Color Doppler signals. Evaluating on femoral and tibial artery scans performed on healthy subjects by an expert ultrasonographer, and comparing to consensus expert ground-truth annotations of inner lumen boundaries, we demonstrate real-time segmentation using the context-aware models and show that they significantly outperform comparable baseline approaches.

Keywords: Deep learning, spatiotemporal attention, vascular ultrasound

1 Introduction

Over 120 million people worldwide are affected by peripheral vascular disease, making it one of the leading causes of morbidity and mortality globally [1]. Vascular ultrasound (US) based on B-mode and Color Doppler imaging is widely used to evaluate luminal narrowing and flow in stenotic vessel segments. Accurate delineation of vessel wall boundaries is crucial for diagnosis and disease prognosis [2], but can be highly challenging due to complex vascular anatomy, visual ambiguity, acoustic imaging artefacts, probe motion, and very small target structures hidden within the US image frame [3]. Automated, real-time segmentation of relevant vessels can aid in clinical assessment while providing a means to improve vascular US imaging workflows and reduce operator dependency.

Prior work on US vessel segmentation have utilized shape and motion models [4,5,6,7] typically requiring initialization with seed points in the first frame.

[†] These authors contributed equally.

* Work done during internship at Philips Research.

To provide additional context, the inclusion of flow information alongside the B-mode image has been proposed [8,9,10,11]. In recent years, deep learning has received increased focus [2,12], with the majority of work on vessel segmentation utilizing UNet/VNet-like models operating on individual frames [13,14]. Incorporating the time dimension, recurrent mechanisms have been combined with convolutional networks as a way to encode temporal memory from image sequences [15,16,17,18,19,20]. However, to date, most studies have focused on segmentation of large carotid [13,14] or coronary [20] arteries using UNet/VNet, and accuracy on small extremity vasculature has not been systematically investigated.

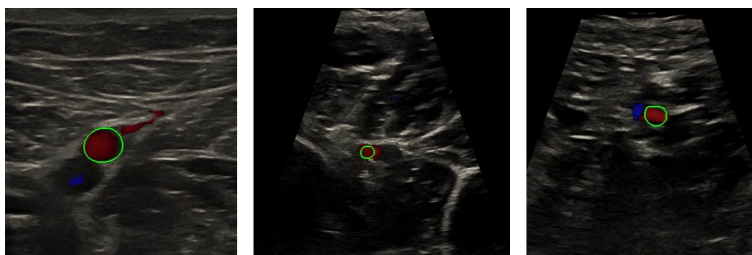


FIG. 1: B-mode and Color Doppler US images of lower-extremity arterial vasculature. Expert ground-truth annotations of inner lumen vessel wall boundaries shown in green. *Left*: femoral artery (~ 5 mm diameter), *Middle*: anterior tibial artery (~ 2 mm diameter), *Right*: posterior tibial artery (~ 3 mm diameter).

Our Contributions. We demonstrate that a spatiotemporally-aware deep learning model is capable of automatic, real-time segmentation of inner lumen vessel boundaries from challenging freehand US sequences (Fig. 1). Improved performance in difficult anatomy, namely small-scale lower-extremity peripheral arterial vasculature, is made possible by leveraging the rich spatiotemporal information available in US and utilizing dual-input B-mode and color flow signals. Our approach aims to simulate the contextual inferencing processes of experienced ultrasonographers, who are trained to recognize temporal signatures in both modalities and attend to small structures of interest while ignoring background.

Specifically, we propose a fully convolutional encoder-decoder network that feeds B-mode and Color Doppler inputs through a series of spatial, temporal, and channel-wise contextual units embedded within each resolution layer. By preserving multi-resolution features as they pass through each unit, the network is able to propagate learned representations temporally across all scales.

Additional contributions of the paper:

1. We systematically study the impact of the multi-scale spatial, temporal, and channel-wise embeddings for segmentation of femoral (4-6 mm diameter) and tibial (2-3 mm diameter) arteries in a series of network ablation experiments.

2. We investigate the utility of exploiting combined B-mode and Color Doppler information compared to B-mode alone, and we evaluate the benefits of domain-specific augmentation on the US small-structure segmentation task.
3. We compare segmentation results against consensus ground-truth annotations from multiple clinical experts, and we demonstrate significant improvements in accuracy using the proposed methods compared to baseline models.

2 Methodology

Model overview. The proposed VESsel NETwork with Spatial, Channel and Temporal context (VesNetSCT+) is illustrated in Fig. 2. The network architecture and implementation details are described below.

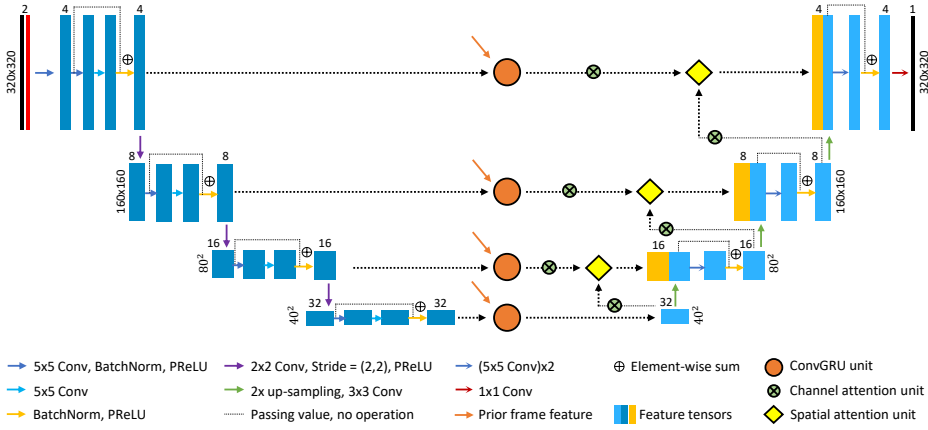


FIG. 2: Network architecture. The model feeds B-mode and Color Doppler inputs through a multi-scale series of spatial, temporal, and feature-wise contextual units embedded in each resolution layer of a fully convolutional encoder-decoder backbone. The design enables efficient learning of multi-modal spatiotemporal context information for challenging small-structure segmentation tasks.

Encoder-Decoder Backbone. Our model uses a UNet/VNet-like[21,22] backbone with a two-channel input to support B-mode and Color Doppler frames. The proposed spatial, temporal, and feature/channel-wise contextual units are sequentially embedded along the residual skip connections[23] in each resolution layer. This design allows the model to aggregate learned representations across multiple spatial scales and time points. We additionally posit that, unlike methods which explicitly modify the backbone network [15,16,17,18], embedding into the skip connections minimizes disruption of gradients along the main path.

Implementation details: B-mode and Color channels are normalized between (0,1) and (-1,1), respectively. We apply batch normalization and PReLU, and we

use resize-up-convolutions [24] in the decoder to minimize checkerboard artifacts. We also reduce the total model size from 30M (original UNet) to 0.3M by opting for a four-layer network backbone capable of real-time inference on clinical US machines. Networks are trained via RMSProp with initial learning rate of 0.0001.

Multi-scale Temporal Gating. To introduce temporal context, a hierarchical series of convolutional gated recurrent units (ConvGRU) [25,26] are embedded between the contracting and expanding paths (round orange blocks in Fig. 2). By replacing dot product operations found in standard GRU with convolutional operations, the learned temporal representations have the inherent spatial connectivity of convolutional networks and are more parameter-efficient [26].

Implementation details: The inputs into the ConvGRU are the feature maps x_t for the current frame t and the hidden states h_{t-1} from the prior time point:

$$z_t = \sigma(W_{hz} * h_{t-1} + W_{xz} * x_t + b_z) \quad (1)$$

$$r_t = \sigma(W_{hr} * h_{t-1} + W_{xr} * x_t + b_r) \quad (2)$$

$$\hat{h}_t = \tanh(W_h * (r_t \odot h_{t-1}) + W_x * x_t + b) \quad (3)$$

$$h_t = (1 - z_t) \odot h_{t-1} + z_t \odot \hat{h}_t \quad (4)$$

where $W_{hz}, W_{xz}, W_{hr}, W_{xr}, b_z, b_r, b$ are learnable convolution kernels and biases. z_t and r_t are internal update and reset gates. The output h_t is computed as a weighted sum of h_{t-1} and candidate activation \hat{h}_t . σ denotes sigmoid activation, \odot denotes element-wise multiplication, and $*$ denotes convolution. All temporal models are trained via truncated backpropagation-through-time (TBTT) with a fixed sequence length of 50 frames. A time window of 1-4 frames is used in the feedforward step and accumulated to compute back-propagation gradients [27].

Multi-scale Spatial Attention. We add soft self-attention gates to provide higher-resolution layers with spatial support from coarse layers. This idea has been shown to improve accuracy on small-structure segmentation tasks [28] and is fully differentiable, unlike hard attention mechanisms based on iterative region proposal and cropping [29]. The spatial self-attention units are introduced in a multi-scale manner along the skip connections, immediately following the temporal and channel operators. The arrangement provides the self-attention gates with access to global spatiotemporal context when learning to suppress irrelevant background and attend to regions of interest.

Implementation details: Within this unit, input feature maps x , and input gating feature maps g from the previous coarse resolution level, are used to derive attention multiplier maps $\alpha: [0, 1] \rightarrow \mathbb{R}^2$. The self-attention maps are multiplied element-wise into each channel of x to produce the output maps \hat{x} :

$$\alpha = \sigma(\psi(\delta(W_x * x + W_g * g + b_\psi))) + b_\psi \quad (5)$$

$$\hat{x}_c = x_c \odot \alpha \quad (6)$$

where σ and δ denote sigmoid and ReLU activations, respectively. W_x, W_g, ψ are weight parameters for the channel-wise $1 \times 1 \times 1$ convolutions, b_ψ, b_g are the bias

terms in the gating unit, and \odot denotes element-wise multiplication between the multiplier and input feature maps at channel c .

Multi-scale Feature-wise Channel Attention. Finally, feature/channel self-attention is incorporated in the skip connections and along the decoder path. Specifically, we employ convolutional block attention modules [30] immediately before each spatial attention gate (round green blocks in Fig. 2). Particularly for tasks involving multiple input modalities, self-attention along the channel dimension offers a mechanism to explicitly model interdependencies between modalities (in our case, the encoded B-mode and Color Doppler input signals).

Implementation details: Given input feature maps x^c with c channels, average- and max-pooling are performed along the channel dimension to produce descriptors $x_{avg}^c, x_{max}^c \in \mathbb{R}^{1 \times 1 \times C}$. These are passed through a shared multi-layer perceptron (MLP) g and element-wise summed. The result, a vector $m_c \in \mathbb{R}^{1 \times 1 \times C}$, is channel-wise multiplied (\otimes) with the input x^c :

$$\hat{x}^c = m_c \otimes x^c \quad (7)$$

$$= \{\sigma(g(x_{avg}^c) + g(x_{max}^c))\} \otimes x^c \quad (8)$$

$$= \{\sigma(W_1(\delta(W_0(x_{avg}^c))) + W_1(\delta(W_0(x_{max}^c))))\} \otimes x^c \quad (9)$$

where σ and δ denote sigmoid and ReLU, and W_0, W_1 are learnable MLP weights.

Domain-specific Augmentation. Extensive data augmentation was applied in training to improve generalizability and robustness to real-world freehand US imaging conditions. Augmentations were defined on training sequences spanning 50 sequential frames, and included: (1) *Spatial augmentation* based on random translation, rotation, scaling, cropping, and horizontal flipping; (2) *Gain/contrast augmentation* based on random adjustment of histogram and time gain compensation curves separately to the B-mode and Color channels; (3) *Color Doppler augmentation*, where channel dropout is applied with fixed probability on the Color inputs to simulate poor Doppler signal due to impaired blood flow; and (4) *Temporal augmentation* by varying the start and end frames, interval between frames, and order of frames (forward or reverse) for each set of 50-frame inputs.

Vascular Ultrasound Data Acquisition. Freehand lower-extremity arterial US exams were performed by an expert vascular sonographer on left and right legs of 7 healthy subjects. Scans were acquired in transverse orientation following standard imaging workflows for diagnostic Duplex ultrasonography [31]. The scans were performed under simultaneous B-mode and Color Doppler modes and spanned the length of the leg, from ankle to groin. In total, 22 exam sequences were acquired, including 13 along the femoral arteries and 9 along the anterior/posterior tibial arteries. All data were collected with a Philips Epiq 7 system and 12 MHz linear transducer (pixel spacing $\sim 0.1\text{mm}$, frame rate $\sim 15\text{Hz}$).

Clinical Expert Ground-Truth Annotation. Expert ground-truth annotations of inner lumen boundaries (Fig. 1) were provided by two experienced vascular sonographers. Consensus ground-truth masks were computed via shape-based averaging of the two sets of individual segmentations [32]. A total of 30,839 consensus-annotated frames were obtained from the 22 femoral and tibial artery exams in this manner. The data were divided according to subject to allow for independent training and testing, and to perform leave-one-out cross-validation.

TABLE 1: Summary of segmentation performance on femoral and tibial test sets.

Model name*	# params	Input channels	Spatial/channel attention	Temporal gating	Time window	Dice score (mean \pm std)
Femoral arteries (4-6 mm diameter)						
Baseline	103k	Bmode	-	-	-	0.775 \pm 0.282
Baseline-L	310k	Bmode	-	-	-	0.788 \pm 0.301
VesNet	103k	Bmode+Color	-	-	-	0.870 \pm 0.150
VesNetS	105k	Bmode+Color	S	-	-	0.881 \pm 0.175
VesNetSC	106k	Bmode+Color	S+C	-	-	0.903 \pm 0.101
VesNet-L	313k	Bmode+Color	-	-	-	0.887 \pm 0.180
VesNetT	259k	Bmode+Color	-	Single	1	0.908 \pm 0.086
VesNetT+	307k	Bmode+Color	-	Multi-scale	1	0.914 \pm 0.065
VesNetST+	309k	Bmode+Color	S	Multi-scale	1	0.919 \pm 0.069
VesNetSCT+	310k	Bmode+Color	S+C	Multi-scale	1	0.925 \pm 0.051
VesNetSCT++	310k	Bmode+Color	S+C	Multi-scale	4	0.927 \pm 0.041
Tibial arteries (2-3 mm diameter)						
Baseline	103k	B-mode	-	-	-	0.133 \pm 0.227
Baseline-L	310k	B-mode	-	-	-	0.164 \pm 0.254
VesNet	103k	Bmode+Color	-	-	-	0.527 \pm 0.336
VesNetS	105k	Bmode+Color	S	-	-	0.564 \pm 0.317
VesNetSC	106k	Bmode+Color	S+C	-	-	0.570 \pm 0.282
VesNet-L	313k	Bmode+Color	-	-	-	0.534 \pm 0.328
VesNetT	259k	Bmode+Color	-	Single	1	0.564 \pm 0.283
VesNetT+	307k	Bmode+Color	-	Multi-scale	1	0.655 \pm 0.211
VesNetST+	309k	Bmode+Color	S	Multi-scale	1	0.664 \pm 0.246
VesNetSCT+	310k	Bmode+Color	S+C	Multi-scale	1	0.671 \pm 0.240
VesNetSCT++	310k	Bmode+Color	S+C	Multi-scale	4	0.679 \pm 0.195

* *Nomenclature.* Baseline: UNet; VesNet: bimodal-input UNet; “-L”: larger network with more channels per layer; “S”: spatial attention; “C”: channel attention; “T”: temporal gating; “+”: multi-scale embeddings; “++”: expanded TBTT window.

3 Results

Validation & Network Ablation Studies.

Temporal, spatial, and channel-wise context: On both femoral and tibial hold-out test data, we saw significant improvements in Dice scores (Table 1) with the addition of temporal, spatial, and feature/channel-wise contextual embeddings alongside bimodal B-mode+Color inputs. For the femoral dataset, the best-performing context-aware model (VesNetSCT++, 0.927 ± 0.041 Dice) demonstrated an improvement of 18 to 20% in comparison to two baseline UNet models of varying sizes (Baseline, 0.775 ± 0.282 Dice; Baseline-L, 0.788 ± 0.301 Dice). Meanwhile, in the tibial arteries, which represented $<0.1\%$ of pixels in each frame, the baseline models failed entirely (Baseline, 0.133 ± 0.227 Dice; Baseline-L, 0.164 ± 0.254 Dice) compared to the context-aware model (VesNetSCT++, 0.679 ± 0.195 Dice).

Multi-scale embeddings: The introduction of temporal/spatial/channel embeddings in a multi-scale manner (VesNetT+) resulted in improved performance compared to equivalent models with the embeddings applied only to the innermost layer of the encoder-decoder backbone (VesNetT), as proposed in [15,16,17,18].

Temporal window: We experimented with the time window for accumulating feed-forward and back-propagation updates when training temporal models using TBTT [27]. Improvements were seen by increasing the window size (VesNetSCT++, time window=4), at the cost of longer training times.

Domain-specific augmentation: Table 2 compares models trained with and without channel dropout on the Color Doppler input. Table 3 compares results with and without temporal augmentation. Overall, we saw that the augmentations resulted in improved test accuracy, which suggests the model’s robustness to the poor Doppler signal quality and varying freehand scanning motions.

TABLE 2: Impact of color augmentation. See Table 1 nomenclature.

Model name	Color Doppler dropout	Dice score
Femoral arteries (4-6 mm diameter)		
VesNetSC	0.0	0.880 ± 0.145
VesNetSC	0.4	0.903 ± 0.101
VesNetSCT+	0.0	0.911 ± 0.087
VesNetSCT+	0.4	0.925 ± 0.051
Tibial arteries (2-3 mm diameter)		
VesNetSC	0.0	0.579 ± 0.312
VesNetSC	0.4	0.570 ± 0.282
VesNetSCT+	0.0	0.676 ± 0.293
VesNetSCT+	0.4	0.671 ± 0.240

TABLE 3: Impact of temporal augmentation. See Table 1 nomenclature.

Model name	Temporal augmentation	Dice score
Femoral arteries (4-6 mm)		
VesNetSCT+	No	0.917 ± 0.117
VesNetSCT+	Yes	0.925 ± 0.051
Tibial arteries (2-3 mm)		
VesNetSCT+	No	0.660 ± 0.245
VesNetSCT+	Yes	0.671 ± 0.240

TABLE 4: Cross-validation results with context-aware models (VesNetSCT+).

Data splits:	1	2	3	4	5	6	7	Mean \pm Stdev
Femoral arteries	0.925	0.853	0.828	0.940	0.935	0.909	0.802	0.885 \pm 0.162
Tibial arteries	0.671	0.782	0.565	0.511	0.646	-	-	0.635 \pm 0.215

Model size and baseline comparisons: Comparing baseline UNet models modified to match the number of parameters as our final proposed models (Baseline-L, 0.3M parameters), a three-fold increase in parameters gave no appreciable improvement in performance (Table 1). This suggests that the improved accuracy of the context-aware models was not due simply to larger network size.

Cross validation: To assess generalization, leave-one-out cross validation was carried out on both datasets using the contextually-aware models (VesNetSCT+). In each split, sequences from one subject were held out for testing (Table 4).

Inference speed: VesNetSCT++ achieved inference speeds of 149.4 ± 4.6 ms (6.7 Hz) on a mobile CPU processor (Intel Core i7 2.6 GHz) and 8.9 ± 0.6 ms (112 Hz) on a mobile GPU (Nvidia RTX 2080). These speeds were significantly faster than those of the Baseline-L UNet model and show that the proposed methods are amenable to real-time processing on hardware used in clinical US machines.

Visualization of Results. Fig. 3 shows examples of the effects of spatiotemporal context on hold-out sequences. In both cases, Dice scores fluctuate less when the contextual mechanisms are introduced. The addition of temporal gating (left panel, comparing VesNet and VesNetT+ models) allows the model to correctly learn pulsatile signatures and ignore confounding Doppler signals from nearby veins. With spatial attention gating (right panel, comparing VesNetT+ and VesNetST+), extremely small tibial arteries are more reliably localized throughout.

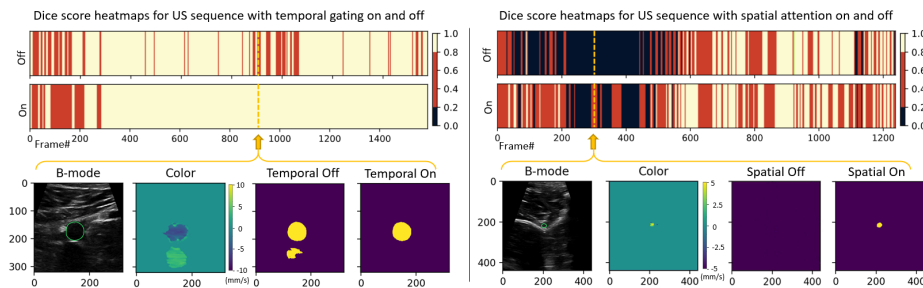


FIG. 3: Visualization of segmentations on hold-out test sequences. *Left:* Temporally-aware model (VesNetT+) outperforms an equivalent model operating in individual frames (VesNet). *Right:* Inclusion of spatial self-attention (VesNetST+) outperforms the same model without spatial attention (VesNetT+).

4 Conclusion

This work presented an efficient deep learning architecture that incorporates multiple strategies for embedding spatiotemporal context to improve segmentation of challenging 2D US image sequences. We applied the methods to small-scale lower extremity arteries from freehand B-mode and Color Doppler scans, and showed strong improvement over baseline models without the added contextual awareness. Future work will investigate the generalizability of these methods on other anatomies where flow and spatiotemporal information are available, and where automatic quantification of vascular measurements is of clinical benefit.

Acknowledgment. The authors thank Elizabeth Brunelle, Barbara Bannister, and Jochen Kruecker for assistance in data acquisition, annotation, and review.

References

1. Bauersachs, R., Zeymer, U., Brière, J. B., Marre, C., Bowrin, K., & Huelsebeck, M. (2019). Burden of coronary artery disease and peripheral artery disease: a literature review. *Cardiovascular therapeutics*, 2019.
2. Moccia, S., De Momi, E., El Hadji, S., and Mattos, L.S. (2018). Blood vessel segmentation algorithms — review of methods, datasets and evaluation metrics. *Computer Methods and Programs in Biomedicine*, 158, 71–91.
3. Liu, S., Wang, Y., Yang, X., Lei, B., Liu, L., Li, S.X., Ni, D., and Wang, T. (2019). Deep learning in medical ultrasound analysis: a review. *Engineering* 5, 261-275.
4. Guerrero, J., Salcudean, S. E., McEwen, J. A., Masri, B. A., and Nicolaou, S. (2007). Real-time vessel segmentation and tracking for ultrasound imaging applications. *IEEE Transactions on Medical Imaging*, 26(8), 1079-1090.
5. Ma, L., Kiyomatsu, H., Nakagawa, K., Wang, J., Kobayashi, E., and Sakuma, I. (2018). Accurate vessel segmentation in ultrasound images using a local-phase-based snake. *Biomedical Signal Processing and Control*, 43, 236-243.
6. Patwardhan, K.A., Yu, Y., Gupta, S., Dentinger, A., and Mills, D. (2012). 4D vessel segmentation and tracking in ultrasound. In 2012 19th IEEE International Conference on Image Processing (ICIP), pp. 2317-2320.
7. Mistelbauer, G., Morar, A., Scherthaner, R., Strassl, A., Fleischmann, D., Moldoveanu, F., and Gröller, E.M. (2021). Semi-automatic vessel detection for challenging cases of peripheral arterial disease. *Computers in Biology and Medicine*, 133, 104344.
8. Keil, M., Oyarzun Laura, C., Drechsler, K., and Wesarg, S. (2012). Combining B-mode and color flow vessel segmentation for registration of hepatic CT and ultrasound volumes. *Eurographics Workshop on Visual Computing for Biology and Medicine*, pp. 57-64.
9. Tamimi-Sarnikowski, P., Brink-Kjær, A., Moshavegh, R., and Jensen, J.A. (2017). Automatic segmentation of vessels in in-vivo ultrasound scans. In *Proceedings of SPIE*, 10137.
10. Moshavegh, R., Martins, B., Hansen, K.L., Bechsgaard, T., Bachmann Nielsen, M., and Jensen, J.A. (2016). Hybrid segmentation of vessels and automated flow measures in in-vivo ultrasound imaging. In *Proceedings of 2016 IEEE International Ultrasonics Symposium (IUS)*, IEEE.

11. Akkus, Z., Carvalho, D.D.B., Van den Oord, S.C.H., Schinkel, A.F.L., Niessen, W.J., De Jong, N., Van der Steen, A.F.W., Klein, S., and Bosch, J.G. (2015). Fully automated carotid plaque segmentation in combined contrast-enhanced and B-mode ultrasound. *Ultrasound in Medicine and Biology*, 41(2), 517–531.
12. Smistad, E. and Løvstakken, L. (2016). Vessel detection in ultrasound images using deep convolutional neural networks. In *Deep Learning and Data Labeling for Medical Applications* (pp. 30-38). Springer, Cham.
13. Zhou, R., Guo, F., Azarpazhooh, R., Hashemi, S., Cheng, X., Spence, J.D., Ding, M., and Fenster, A. (2021). Deep learning-based measurement of total plaque area in B-mode ultrasound images. *IEEE Journal of Biomedical and Health Informatics*, doi: 10.1109/JBHI.2021.3060163.
14. Zhou, R., Fenster, A., Xia, Y., Spence, J.D., and Ding, M. (2019). Deep learning-based carotid media-adventitia and lumen-intima boundary segmentation from three-dimensional ultrasound images. *Medical Physics*, 46(7), 3180-3193.
15. Gao, Y., Phillips, J., Zheng, Y., Min, R., Fletcher, P., Gerig, G. Fully convolutional structured LSTM networks for joint 4D medical image segmentation. In: *Proceedings ISBI 2019*, pp. 1104–1108. IEEE, (2019).
16. Milletari, F., Rieke, N., Baust, M., Esposito, M., Navab, N. CFCM: Segmentation via Coarse to Fine Context Memory. *Proc MICCAI*. 667-74, (2018).
17. Arbellet, A., Raviv, T. R. Microscopy Cell Segmentation Via Convolutional LSTM Networks. *Proc ISBI*, (2019).
18. Webb, J.M., Meixner, D.D., Adusei, S.A., Polley, E.C., Fatemi, M., and Alizad, A. (2020). Automatic deep learning semantic segmentation of ultrasound thyroid cineclips using recurrent fully convolutional networks. *IEEE Access*, 9, 5119-5127.
19. Duque, V.G., Chanti, D.A., Crouzier, M., Nordez, A., Lacourpaille, L., and Mateus, D. (2020). Spatio-temporal consistency and negative label transfer for 3D freehand US segmentation. *International Conference on Medical Image Computing and Computer-Assisted Intervention (MICCAI)*, pp. 710-720.
20. Mirunalini, P., Aravindan, C., Thamizh Nambi, A., S. Poorvaja, and V. Pooja Priya. (2019). Segmentation of coronary arteries from CTA axial slices using deep learning techniques. *IEEE Region 10 International Conference (TENCON)*, pp. 2074-2080.
21. Ronneberger O, Fischer P, and Brox T. (2015). U-Net: Convolutional networks for biomedical image segmentation. In *International Conference on Medical Image Computing and Computer-Assisted Intervention (MICCAI)*, pp. 234-241. Springer, Cham.
22. Milletari, F., Navab, N., and Ahmadi, S. (2016). V-Net: Fully Convolutional Neural Networks for Volumetric Medical Image Segmentation. *4th International Conference on 3D Vision*.
23. He, K., Zhang, X., Ren, S., and Sun, J. (2016). Deep residual learning for image recognition. In *Proceedings of the IEEE Conference on Computer Vision and Pattern Recognition (CVPR)*, pp. 770-778.
24. Odena, A., Dumoulin, V., and Olah, C. (2016). Deconvolution and checkerboard artifacts. <http://distill.pub/2016/deconv-checkerboard/>.
25. Siam, M., Valipour, S., Jagersand, M., and Ray, N. (2017). Convolutional gated recurrent networks for video segmentation. In *IEEE International Conference on Image Processing (ICIP)*, pp. 3090-3094.
26. Ballas, N., Yao, L., Pal, C. and Courville, A. (2015). Delving deeper into convolutional networks for learning video representations. *arXiv:1511.06432*.

27. Williams, R.J. and Zipser, D. (1995). Gradient-based learning algorithms for recurrent networks and their computational complexity. In Y. Chauvin and D.E. Rumelhard (Eds.), *Backpropagation: Theory, Architectures, and Applications*.
28. Oktay, O., Schlemper, J., Folgoc, L.L., Lee, M., Heinrich, M., Misawa, K., Mori, K., McDonagh, S., Hammerla, N.Y., Kainz, B. and Glocker, B. (2018). Attention U-Net: Learning where to look for the pancreas. arXiv:1804.03999.
29. Mnih, V., Heess, N., Graves, A., and Kavukcuoglu, K. (2014). Recurrent models of visual attention. arXiv:1406.6247.
30. Woo, S., Park, J., Lee, J. Y., and Kweon, I. S. (2018). Cbam: Convolutional block attention module. In *Proceedings of the European conference on computer vision (ECCV)* (pp. 3-19).
31. Strandness Jr., D.E. *Duplex Scanning in Vascular Disorders, Third Edition*. Lippincott Williams & Wilkins, Philadelphia, Pennsylvania, 2001.
32. Rohlfing, T. and Maurer Jr., C.R. (2005). Shape-based averaging for combination of multiple segmentations. In *International Conference on Medical Image Computing and Computer-Assisted Intervention (MICCAI)*, pp. 838-845. Springer, Cham.